An inverse method for noninvasive material discrimination with multi-energy X-ray radiography

Andrew J. Gilbert[a], Benjamin S. McDonald[a], Mark R. Deinert[b]

[a]*Pacific Northwest National Laboratory, Richland, WA 99354*
[b]*Colorado School of Mines, Golden, CO 80401*

Abstract. Active X-ray inspections have great potential for non-invasive detection of illicit materials. Dual-energy X-ray radiography, in particular, has been used to determine material composition by utilizing the energy-dependence of the X-ray attenuation coefficients. However, current implementations of this method are limited in their ability to determine the material composition of composite objects. Here we present an inverse algorithm that uses multi-energy X-ray radiography data to non-invasively reconstruct the content of a container. A critical feature of the current contribution is that material identification can be performed using conventional detectors, and X-ray spectra with different endpoint energies produced by varying nothing more than the tube voltage. Adaptive regularization is used to increase the accuracy of material estimations from multi-energy data sets. The utility of these methods is demonstrated with experimentally acquired radiographs obtained using a tunable X-ray source that produces spectra with endpoint energies between 100-450 keV. The object inspected is a scale-model of a nuclear materials storage container, composed of 3D-printed plastic and stainless-steel spheres inside a thin-walled steel container. Reconstructions of the steel sphere thicknesses are within a root-mean-square error of 0.37 cm.

Keywords: X-ray radiography, inverse problems, materials characterization

Corresponding authors. MR Deinert, Colorado School of Mines, email: mdeinert@mines.edu; BS McDonald, Pacific Northwest National Laboratory, email: Benjamin.Mcdonald@pnnl.gov.

Introduction. Recent arms control treaties, including New START, have resulted in the reduction of strategic nuclear weapons in the United States and Russia [1-3]. As stockpiles are further reduced under current and future arms treaties, noninvasive techniques that can accurately account for nuclear material from dismantled weapons become increasingly important. Measurements that can accurately, and noninvasively, determine material composition are essential to confirming that a weapon has been dismantled as agreed, and to aid in the nonproliferation of nuclear materials [4, 5].

In general, the use of spectral information to aid in quantitative X-ray radiography has been widely applied since dual-energy body scans were introduced to help distinguish between bone and tissue, e.g., [6]. More recently, dual-energy radiography has been used in security inspections in an attempt to detect drugs, explosives, and high-atomic-numbered materials [7-9]. However, a key limitation with the dual-energy technique is that it can only determine two unknowns. Two scans is the limit in practice since models for the components of the X-ray attenuation coefficients are calculated as functions of only density

and atomic number (Z). Therefore, dual-energy radiography can be used to determine an average density and atomic number for a given X-ray path length between the source and detector plane [10]. This is a significant limiting factor for detection of nuclear materials because higher-Z materials can be shielded by lower-Z materials so that the average Z is below some threshold. Dual-mode systems that use both neutron and X-ray radiography have been shown to improve material sensitivity [11, 12], but at the cost of increased system complexity.

An alternate approach to dual-mode X-ray systems is to increase the amount of spectral information available for material discrimination. It was previously shown that energy-discriminating X-ray detectors can be used to differentiate between high density and nuclear materials in small, composite objects (i.e. baggage) using single scans and an inverse algorithm formulation [13]. Further, simulated dual-mode high-energy X-ray and neutron radiography have shown promise for material discrimination in large objects [14]. It has also been shown that this approach can be used in combination with tomography to verify the presence of nuclear material in warheads [15]. Here we show that an inverse algorithm can be used to discriminate several materials using standard (non-energy-discriminating) detectors and multiple X-ray spectra generated by varying the tube voltage. We demonstrate the method using a scale model of a nuclear materials storage container, composed of two stainless steel spheres within a 3D-printed plastic mold contained within a thin-walled steel container.

Methods. The interaction of an X-ray beam with an object comprised of *K* materials can be described using a modified form of Beer's law:

$$\Phi(\vec{\rho}, E) = \Phi_0(E)\exp[-\textstyle\sum_{k=1}^{K} \mu_k(E)\rho_k] + \Phi_{scatter}(E) \quad (1)$$

Here, $\Phi(\vec{\rho}, E)$ [X-ray·cm^{-2}·keV^{-1}] is the X-ray spectral fluence incident on the detector plane for a given X-ray source spectrum $\Phi_0(E)$ [X-ray·cm^{-2}·keV^{-1}]. The energy-dependent mass attenuation coefficient for material *k* is μ_k [cm^2·g^{-1}], ρ_k [g·cm^{-2}] is its areal density, and $\Phi_{scatter}(E)$ [X-ray·cm^{-2}·keV^{-1}] is the fluence from X-rays that are scattered onto the image plane. The vector $\vec{\rho}$ contains the areal densities for the *K* materials of interest. The mass attenuation coefficients can be found readily online [16] and are shown for a few materials in Fig. 1. Scattered x-rays affect radiographs and care is taken to limit their effects when radiography systems are designed.

The radiography system response is given by:

$$\vec{d}_\ell(\vec{\rho}) = \frac{c\,\vec{R}_\ell(\vec{\rho})}{c\prime\,\vec{R}_\ell(\vec{0})} \quad (2)$$

where,

$$\vec{R}_\ell(\vec{\rho}) = \int_E \overrightarrow{\Phi_\ell}(\vec{\rho}, E)\varepsilon(E)dE \quad (3)$$

Equation (3) describes the response of the detector to a spectral X-ray fluence. Here, both the response and the fluence are shown as pixelwise vectors where the values in $\overrightarrow{\Phi_\ell}(\vec{\rho}, E)$ are given by Eq. (1). Here, $\varepsilon(E)$ is the efficiency of the detector at energy E [17] and the index ℓ denotes a given X-ray source spectrum. The system response $\vec{d}_\ell$ is the ratio of the detector response with an object present to that with no object present, i.e., $\vec{\rho} = \vec{0}$, and $\boldsymbol{C}$ and $\boldsymbol{C}'$ are the respective convolution matrices. The ratio is taken elementwise for the vector of detector responses $\vec{R}_\ell(\vec{\rho})$, see Supplementary Note 1 for additional details.

For a radiography system, a finite spatial resolution can be modeled with a point-spread-function (PSF) that is Gaussian in shape. It was found for this system that a dual-Gaussian PSF performed better in modeling the effect, one of which is narrower than the other. The narrow Gaussian likely captures the spatial resolution of the radiographic detector while the wider Gaussian captures the broadening due to flux scattered off the back wall. The finite spatial resolution is accounted for with $\boldsymbol{C}$ and $\boldsymbol{C}'$, the respective 2-D convolution matrices for the object and no-object radiographs. The convolution matrices operate on the vector of detector pixel responses $\vec{R}_\ell(\vec{\rho})$. Additional information is given in Supplementary Note 1.

In practice, determining material composition from an X-ray inspection can be difficult since the material attenuation coefficients, μ, show limited uniqueness and bremsstrahlung X-ray sources have large overlapping regions in energy. Regularization [18, 19] can be used to improve optimization results for such ill-posed problems, and amounts to adding additional information to the objective function to be minimized:

$$Q(\vec{\rho}; \alpha, \beta, \vec{\rho}_{n-1}) = \frac{1}{2}\left\| \frac{\vec{d}(\vec{\rho}) - \vec{d}_{obs}}{\sqrt{\vec{d}(\vec{\rho}_{n-1})}} \right\|^2 + \alpha \sum \sqrt{(\boldsymbol{D}_i\vec{\rho})^2 + (\boldsymbol{D}_j\vec{\rho})^2 + \beta} \quad (4)$$

The first term on the right is the least-squares misfit and the second term is the total variation regularization, which includes a weighting term α that varies the strength of the regularization. Here, $\vec{d}(\vec{\rho})$ is the forward predicted detector response and $\vec{d}_{obs}(\vec{\rho})$ is its observed response. These data vectors are a concatenation of data for all pixels at each source X-ray spectrum, i.e., $\vec{d}(\vec{\rho}) = [\vec{d}_1(\vec{\rho}),\ \vec{d}_2(\vec{\rho}), \ldots, \vec{d}_M(\vec{\rho})]$, where M is the total number of X-ray spectra that the object is scanned with. The optimization is then done by solving for a set of material densities at each detector pixel that results in a best match to the observed response at that pixel and X-ray spectrum. Both $\boldsymbol{D}_i$ and $\boldsymbol{D}_j$ in the second term on the right are block Toeplitz matrices and that the operations performed on $\vec{\rho}$ are convolutions. The misfit term is weighted by the square root of the elements from the previous iteration's $\vec{\rho}_{n-1}$, where n is the current iteration of the optimization, and the ratio is taken elementwise. This is done so that the variance in the large count data does not overweight the misfit in the norm, as has been shown effective previously [13].

The total variation regularization term smooths the solution by penalizing Q for sharp variations between neighboring pixels. This is accomplished by taking backwards finite differences of $\vec{\rho}$ in the row i and column j dimension of the image by using finite difference matrix operators $\mathbf{D}_i$ and $\mathbf{D}_j$, respectively [18, 19]. Both $\mathbf{D}_i$ and $\mathbf{D}_j$ are constructed so that the variation of material estimates across the image boundaries has no effect on the total variation (a symmetric boundary condition). This is done by setting rows in $\mathbf{D}_i$ or $\mathbf{D}_j$ that correspond to components of $\vec{\rho}$ on the image border to 0. The squares of the matrix vector product $(\boldsymbol{D}_i\vec{\rho})^2$ are taken element-wise. The term β ensures that Q is differentiable for all possible sets of $\vec{\rho}$ and is set to 1 in this work.

A Newton-type algorithm is used to optimize Eq. (4). Here, Q is optimized iteratively by approximating it as a locally quadratic function at each iteration and minimizing this approximation. In order to use this method, the first derivative (gradient) and second derivative (Hessian) of Q, or an approximation thereof, must be found at each Newton iteration. The gradient of the misfit and regularization terms are calculated analytically. The second derivative of the misfit term is approximated with the Jacobian matrix, i.e. the Gauss-Newton algorithm [18]. This is more efficient than calculating the full Hessian and was found to perform comparably to when the full analytical Hessian matrix was used. The full Hessian is calculated for the regularization term. For all the following results, regularized or unregularized, a non-negativity constraint is put on the solution by using the projected gradient, reduced Hessian algorithm [18]. This modification to the Newton algorithm prevents updates to $\vec{\rho}$ from moving into negative density space and projects any stray component of $\vec{\rho}$ from negative-space to 0.

The regularization weighting term α is selected adaptively in the algorithm, utilizing the unbiased predictive risk estimator (UPRE); the same as what was previously shown effective [13]. This method requires an estimation of the noise in the image data. It is found that the noise in the weighted image data, i.e. Eq. (3), is approximately normally distributed with a standard deviation of 0.0014. This value is used for the calculation of the UPRE, where an outer loop is put on the optimization algorithm that varies α to find a minimum of the UPRE. The Matlab function *fminbnd* is used for this outer optimization, which uses the golden search method to find an optimal $\log(\alpha)$ to a tolerance of 0.05. Additional information is contained in Supplementary Note 2.

An initial guess for $\vec{\rho}$ is set in the algorithm to the zero vector, $\vec{0}$, and a stopping criteria for the Newton iterations is set to be when the maximum change in any value of $\vec{\rho}$ is less than 10^{-4}. The algorithm is implemented in Matlab.

Experimental setup and radiography. The bremsstrahlung X-ray source used for this work was a Comet MXR-451/26. It has a tungsten target at a 30° takeoff angle with 5 mm integrated beryllium filtering, a variable source spot size of 2.5 mm or 5.5 mm, and is tunable from 100 to 450 kVp with a maximum current of 4.9 A. The detector was a PerkinElmer XRD-0822-AP, which has a 140 μm thick Gd_2O_2S:Tb (GOS) scintillator and a 1024×1024 pixel matrix of 200 μm pitch. The signal output is digitized to 16 bits and the

readout electronics are shielded to reduce noise. For the purposes of the image model, Eq. (3), the bremsstrahlung spectrum $\Phi_{0,\ell}$ was modeled in MCNP5 [20] and ε was estimated based on the total attenuation expected in the GOS scintillator. Additional information on the radiographic setup can be found in Supplementary Note 3.

The object inspected was a scale-model of an AT400R nuclear materials storage container [21]. It is composed of two 1.9 cm diameter spherical stainless-steel spheres held in a plastic (ABS) cylinder which is placed in a steel can. The plastic piece (ABS-P400, Stratasys) was made with a 3-D printer and had a diameter of 10.1 cm with cavities to hold the spheres. This object is shown in Fig. 2a, along with the experimental setup, Fig. 2b. The radiograph of the object is shown in Fig. 3. Here, the dark current image has been subtracted and the flat-field (no object) image divided from the object image.

Estimation of the $\Phi_{scatter}$ *term*. Scattering is estimated by comparing a simulated data set using a ray-tracing attenuation data model without a scattered flux contribution to the observed data. This is similar to other work that estimated a scatter term based on the observed flux on heavily shielded image boundaries [22]. The difference between the real and simulated data is calculated for each incident spectrum and the difference is fit with a 2-D second-order polynomial. Additional information on this estimation can be found in Supplementary Note 4.

Error Calculations. The root mean square error (RMSE) is used as a measure of goodness-of-fit of the material estimates from the algorithm to an approximation of the actual steel sphere thicknesses. The RMSE is calculated here by comparing the steel sphere thicknesses output from the inverse algorithm to a theoretical spherical profile at the same locations as the steel spheres in the radiograph. This theoretical profile is used in the absence of a true ground-truth for the steel sphere thicknesses. The RMSE is then the average over all steel-estimated pixels in the region of the steel spheres.

Results. Figure 4a shows the results for experimentally obtained radiographs when four X-ray spectra of 150, 250, 300, and 450 keV endpoint energies are used. Results both with and without regularization are shown. The chosen basis material set is {steel, aluminum, ABS plastic}, consistent with the actual scale-model composition. The regularization weighting factor α was adaptively chosen, and was found to be $10^{-7.1}$. The results with regularization show the steel spheres with high contrast, and the profile of the steel can is visible in the steel estimation, indicating sub-millimeter precision with these methods. Even so, the maximum steel thickness of the steel spheres is underestimated by about 0.28 cm, at 1.63 cm when it should be 1.9 cm. In contrast, the estimations without regularization are very noisy, especially in the ABS and Al results, and the steel sphere thickness is more significantly underestimated by 0.88 cm, at 1.02 cm when it should be 1.9 cm.

Figure 4b shows the material estimations using only two X-ray spectra with endpoint energies of 350 and 450 keV. Here, the three-basis material set is still used and regularization shows its utility in obtaining an estimated material thickness to reasonable accuracy with an otherwise underdetermined system, including sensitivity to the small steel can thickness. The value for α, picked adaptively, was $10^{-6.7}$. It might appear counter

intuitive that two scans (X-ray endpoints) can be used to solve for three materials. However, regularization introduces additional information into the optimization algorithm that allows for an accurate reconstruction relative to the target material set. Here, the maximum steel sphere thickness is underestimated by about 0.54 and 0.55 cm for the regularized and unregularized cases, even though the unregularized result is considerably noisier. In this case, the RMSE better captures the difference between these results. See Table I for a summary of the experimental results.

The number of materials that can be reconstructed is limited by the number of spectra, the energy dependent mass attenuation coefficients of the materials and the regularization. The inverse approach is demonstrated here for 3 materials. However, reconstruction of more could be possible, particularly when the unique features of the X-ray attenuation coefficients can be observed.

In both the multi- and dual-endpoint cases, shown in Fig. 4, regularization improves the prediction of steel thickness, and eliminates the estimated presence of aluminum. However, even with regularization the amount steel is underpredicted by ~14%. The dominant reason for this under-prediction comes from the scattering of X-rays (from the inspected object and room) onto the plane where the image of the steel spheres is generated. This has the effect of increasing the X-ray flux at these locations and making it appear as though there is less attenuation from the sphere than is really the case. As the thickness of the steel increases this becomes more of an issue because the unattenuated flux through the spheres will approach the magnitude of the scattered flux. Both effects would be reduced with the use of an anti-scatter grid.

Conclusions. The results presented here show that multi-energy radiography can be used in conjunction with an inverse algorithm and regularization to determine the material composition of objects using conventional X-ray detectors. The method described can be used with conventional radiographic systems and provides an important advance for detection of nuclear materials in containers and treaty verification [e.g. 23, 24]. Though the methods presented here were for quantification of materials in small containers with mid-energy X-ray scans they could also be used with higher-energy inspections of larger items, such as cargo containers, trucks, etc. The algorithms would still rely on the use of a set of suspected materials, though flexibility could be built into the methods for more complex objects.

Acknowledgements. This work was partially supported by the U.S. Department of Energy, National Nuclear Security Agency, Office of Defense Nuclear Non-Proliferation Research and Development. A. J. Gilbert is supported by the Office of International Nuclear Safeguards. A portion of the research was performed using PNNL Institutional Computing at Pacific Northwest National Laboratory. Pacific Northwest National Laboratory is operated for the U.S. Department of Energy by Battelle under Contract DE-AC05-76RL01830. The external release identifier for this publication is PNNL-SA-122169.

References

1. *Strategic Arms Reductions Treaty: Treaty Text*, 1991.
2. *Strategic Offensive Reductions Treaty: Treaty Text*, 2002.

3. *New Strategic Arms Reduction Treaty: Treaty Text*, 2010.
4. Medalia, J., *Detection of nuclear weapons and materials: Science, technologies, observations*, C.R. Service, Editor 2008, Congressional Research Service p. 12-13.
5. Nichol, J., *Central Asia's New States: Political Developments and Implications for U.S. Interests*, 2002, LIBRARY OF CONGRESS WASHINGTON DC CONGRESSIONAL RESEARCH SERVICE.
6. Mazess, R., H. Barden, J. Bisek, J. Hanson, *Dual-energy x-ray absorptiometry for total-body and regional bone-mineral and soft-tissue composition.* The American Journal of Clinical Nutrition, 1990. **51**(6): p. 1106.
7. Chen, G., G. Bennett, D. Perticone, *Dual-energy X-ray radiography for automatic high-Z material detection.* Nuclear Instruments and Methods in Physics Research B, 2007. **261**(1-2): p. 356-359.
8. Moulin, V., V. Rebuffel, M. Antonakios, R. Sauze, J. Gorius. *X-ray imaging modalities for nuclear waste drums inspection*. in *Proceedings of the 16th World Conference on Non-Destructive Testing*. 2004. Montreal, Canada.
9. Runkle, R., T. White, E. Miller, J. Caggiano, B. Collins, *Photon and neutron interrogation techniques for ... in air cargo: A critical review* Nuclear Instruments and Methods in Physics Research A, 2009. **603**(3): p. 510-528.
10. Ogorodnikov, S., V. Petrunin, *Processing of interlaced images in 4–10 MeV dual energy customs system for material recognition.* Physical Review Special Topics-Accelerators and Beams, 2002. **5**(10): p. 104701.
11. Liew, S.V., *X-ray and neutron interrogation of air cargo for mobile applications.* Nuclear Instruments and Methods in Physics Research Section A, 2015. **784**: p. 417-422.
12. Cutmore, N.G., *Development and commercialization of a fast-neutron/x-ray Cargo Scanner*, in *IEEE International Conference on Technologies for Homeland Security (HST)*2010.
13. Gilbert, A.J., B.S. McDonald, S.M. Robinson, K.D. Jarman, T.A. White, M.R. Deinert, *Non-invasive material discrimination using spectral x-ray imaging.* Journal of Applied Physics, 2014. **115**: p. 154901.
14. Gilbert, A.J., B.S. McDonald, M.R. Deinert, *Advanced algorithms for radiographic material discrimination and inspection system design.* Nuclear Instruments and Methods in Physics Research B, 2016. **385**: p. 51-58.
15. Kemp, R.S., A. Danagoulian, R.R. Macdonald, J.R. Vavrek, *Physical cryptographic verification of nuclear warheads.* Porceedings of the National Academy of Sciences, 2016. **113**(31): p. 8618-8623.
16. *ENDF/B-VII evaluated photoatomic data*, Los Alamos National Laboratory.
17. Knoll, G., *Radiation Detection and Measurement*2000: John Wiley & Sons, Inc.
18. Vogel, C.R., *Computational Methods for Inverse Problems*2002, Philadelphia: Society for Industrial and Applied Mathematics.
19. Bardsley, J.M., A. Luttman, *Total variation-penalized Poisson likelihood estimation for ill-posed problems.* Advances in Computational Mathematics, 2009. **31**(1-3): p. 35-59.
20. X-5 Monte Carlo Team, *A General Purpose Monte Carlo N-Particle Transport Code*, 2003, Radiation Safety Information Computational Center: Los Alamos, NM.
21. McDonald, B., T. White, H. Seifert, S. Robinson, K. Jarman, A. Misner, *Verification of Declared Attributes in a Materials Storage Scenario with Radiation Imaging Methods*,

2014.
22. Siewerdsen, J.H., M.J. Daly, B. Bakhtiar, D.J. Moseley, S. Richard, H. Keller, D.A. Jaffray, *A simple, direct method for x−ray scatter estimation and correction in digital radiography and cone−beam CT.* Medical physics, 2006. **33**(1): p. 187-197.
23. Kemp, R.S., A. Danagoulian, R.R. Macdonald, and J.R. Vavrek, *Physical cryptographic verification of nuclear warheads.* PNAS, 2016. 113 (31): p. 8618-8623.
24. Helca, J.J., A. Danagoulian, *Nuclear disarmament verification via resonant phenomena.* Nature Communications*,* 2018, 9: 1259.

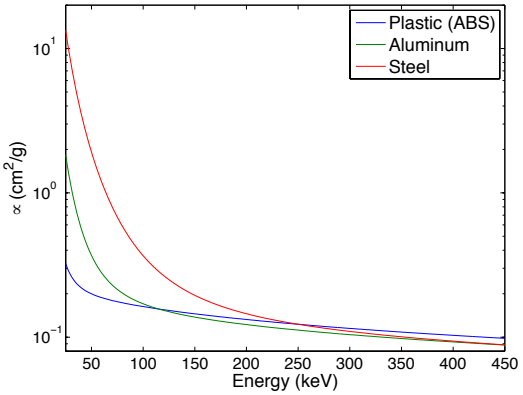

Figure 1. Mass attenuation coefficients for a few materials of interest. The unique energy dependence of these coefficients is the basis for discriminating one material from another.

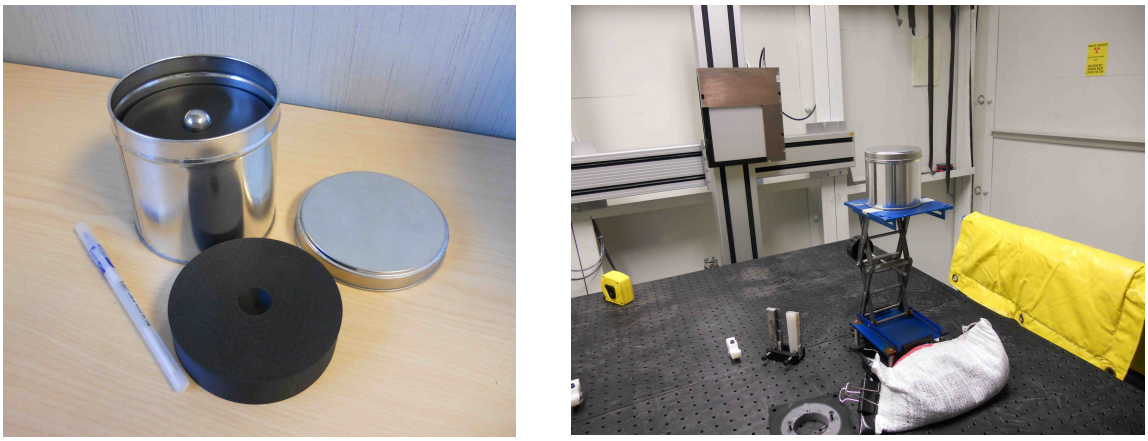

(a) (b)

Figure 2. Experimental system and beam floor. (a) The scale-model object used in these inspections. It is composed of a thin-walled steel container with stacked, 3D printed ABS pieces, which have two spherical cavities to set the steel spheres into. (b) The experimental setup with the object and detector visible. The source is located behind the camera, along the axis from the object to the detector.

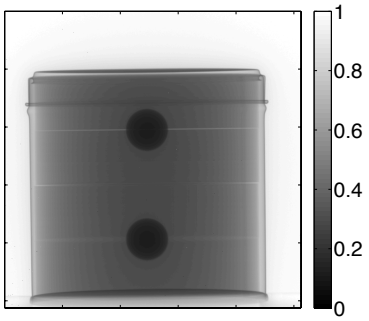

Figure 3. An X-ray image of the scale-model object used in this work. The flat-field correction has been made to remove non-uniformities in the image detector response.

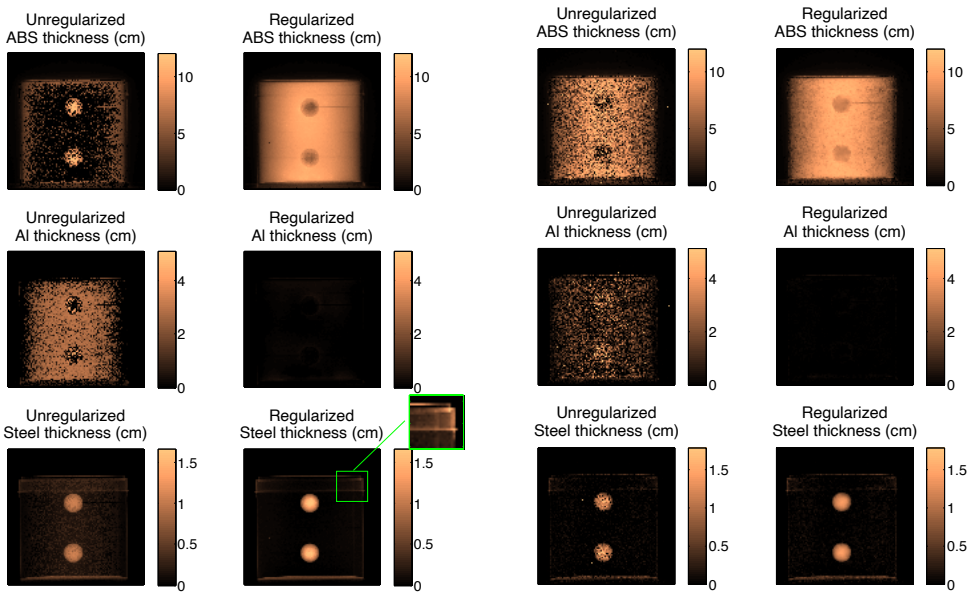

Figure 4. Estimated material compositions from the X-ray inspections. (a) Results from a scan of 150, 250, 300, and 450 keV endpoint energies, with and without regularization. The unregularized results show significant material confusion between the ABS and Al, which is removed with the addition of regularization (there is no Al in the inspected object). The inlay from the regularized steel estimate shows good sensitivity in reconstructing the ~1 mm thicknesses of the steel container wall. (b) Results from a scan with only the 350 and 450 keV endpoint energies show utility of the method to accurately solve an otherwise underdetermined system (3 unknowns from 2 X-ray scans). The steel material error is summarized in Table I.

Table I. The root mean square error (RMSE) of the estimated steel thicknesses compared to an approximation of the actual steel sphere thicknesses. The approximation of the actual steep thicknesses is given by theoretical spherical profiles on the image plane in the same location as those in the radiograph.

Endpoint Set (keV)	Reg. RMSE Steel (cm)	Unreg. RMSE Steel (cm)
150, 250, 300, 450	0.37	0.58
350, 450	0.45	0.66

Supplementary Information

An inverse method for noninvasive material discrimination with multi-energy X-ray radiography

Andrew J. Gilbert, Benjamin S. McDonald, Mark R. Deinert

Supplementary Note 1. Generation of the convolution operator. Measurement of the system spatial resolution and generation of the convolution operator matrix used in Eq. (2) was completed using radiography data of an edge profile, specifically step wedges of heavily attenuating materials, lead and steel. The image used is shown in Fig. S1a, along with the locations of the profiles used in the analysis. The line profile is taken as the column average of the region shown in Fig. S1a. The line spread function is then found by taking the finite difference of a profile of the lead step edge across image column, i.e., $I(i, j+1) - I(i, j)$, as shown as "data" in Fig. S1b.

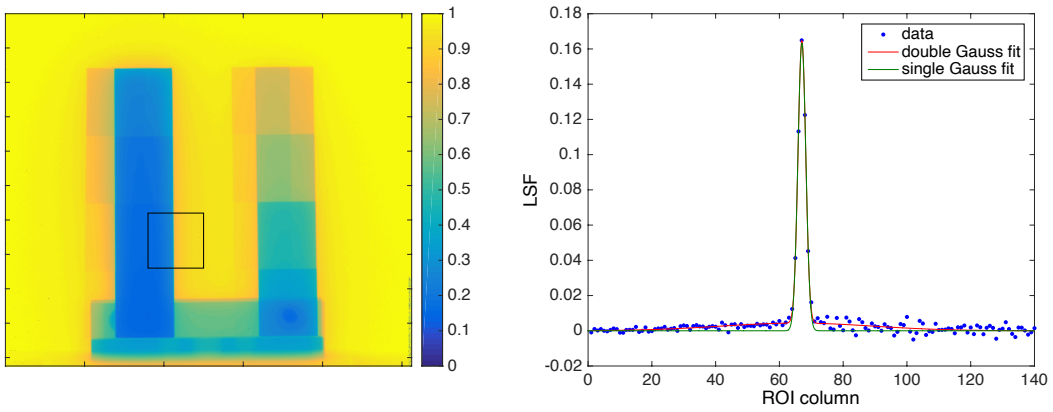

(a) (b)

Figure S1: (a) The 350 keV endpoint image data of lead (left) and steel (right) step wedges. The region of interest (ROI) shown in black is the used for the generation of the line spread function (LSF). (b) The LSF is generated by taking the finite difference of the of the column-averaged profile in the ROI. The maximum in the LSF is at the edge of the heavily attenuating lead object.

Figure S1b also shows functional fits to the LSF data. A double Gaussian fit is able to better represent the long tail observed in the LSF for this imaging system, e.g., reducing the RMSE from 0.02 for the single Gaussian to 0.0006 for the double Gaussian. This long

tail could be due to the effective source spot size increasing due to the considerable, 1/2 in., steel filter put on the source, especially since no beam collimation was used. Backscatter off the back wall may also contribute to this, as was also observed in modeling studies. The dual Gaussian used for fits to the LSF is given by:

$$F(x) = \mathrm{A}_1 \exp\left[\frac{(x-\mu_1)^2}{2\sigma_1^2}\right] + A_2 \exp\left[\frac{(x-\mu_2)^2}{2\sigma_2^2}\right] \quad \text{(S1)}$$

where μ_1 and μ_2 for the two Gaussian functions are held at 0. The other parameters are allowed to vary to maximize the fit. Table S1 shows the parameters used in the generation of the point spread function (PSF) and the resulting convolution matrix. In practice, it was found that the values determined for σ_2 using the LSF alone did not well match the observed data. Therefore, this parameter was modified by visual inspection, by comparing observed data of the object and that modeled and selecting the value that resulted in edge behavior that looked consistent.

Table S1: LSF dual-Gaussian parameters used to generate the point spread function for each inspection endpoint energy.

Parameter	150 keV	200 keV	250 keV	300 keV	350 keV	400 keV	450 keV
A_1/A_2	57.8	50.6	51.8	49.5	49.8	46.5	45.1
$\sqrt{2}\,\sigma_1$	2.22	2.28	2.29	2.32	2.43	2.42	2.45
$\sqrt{2}\,\sigma_2$	72.2	75.5	80.5	82.7	86.6	86.5	87.9

The point spread function (PSF) is related to the LSF through a Radon transform.

$$LSF(x) = \int_{-\infty}^{\infty} PSF(x,y)dy \quad \text{(S2).}$$

Symmetry in the LSF is assumed here (i.e., the LSF will be the same at any edge angle), and this is used to generate the PSF by using the inverse Radon transform, specifically ramp-filtered back projection. A resulting PSF is shown in Fig. S2. It is also assumed that the PSF is shift-invariant. Shift-variance of the LSF was confirmed by observing consistency in the LSF at various edge locations.

Using the generated PSF at each X-ray inspection endpoint energy, the two-dimensional convolution operator matrix $\boldsymbol{C}$ used in Eq. (2) is formulated by creating a sparse block diagonal matrix of $NM \times NM$, where N is the number of pixels in the image data and M is the number of spectra used in the inspection. Each block of the matrix is then the convolution matrix for the given inspection endpoint energy, defined so that that each row of the block describes the blurring of the response in a given pixel to neighboring pixels.

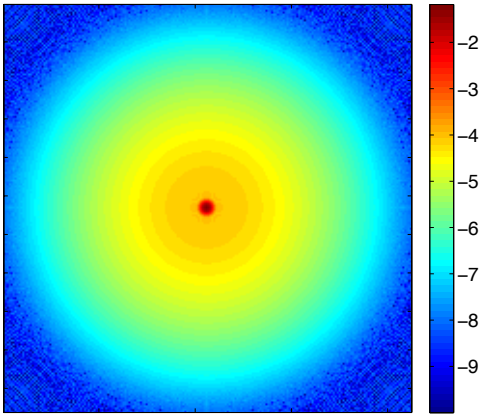

Figure S2: The PSF calculated from the experimentally determined LSF (in log scale). The extent of the x and y axes are effectively 35 pixels. This figure shows the PSF at a higher spatial resolution for a better observation of the PSF shape.

The PSF has no effect on a uniform flatfield image so $\boldsymbol{C}'$ in Eq. (2) is assumed to be ~1.

Supplementary Note 2. Adaptive regularization parameter selection. The unbiased predictive risk estimate (UPRE) method as given by Vogel [1] and Bardsley [2] is used here for adaptive selection of α within the optimization algorithm. The interested reader is pointed to these references for further information regarding this method for α selection, though we provide a brief description here. This method seeks a statistical estimator of the predictive risk:

$$\frac{1}{n}\|\vec{p}_\alpha\|^2 = \frac{1}{n}\left\|\vec{d}(\vec{\rho}_\alpha) - \vec{d}(\vec{\rho}_{true})\right\|^2 \quad \text{(S3)}$$

where $\vec{\rho}_\alpha$ is the regularized solution vector from the algorithm, $\vec{\rho}_{true}$ is the true material composition, and n is the number of elements in $\vec{\rho}_\alpha$. Since $\vec{\rho}_{true}$ is not available to directly calculate the predictive risk, an estimator, the UPRE, is given [1]:

$$U(\alpha) = E\left(\frac{1}{n}\|\vec{p}_\alpha\|^2\right) = \frac{1}{n}\|\vec{r}_\alpha\|^2 + \frac{2\sigma^2}{n}trace(\boldsymbol{A}_\alpha) - \sigma^2$$

$$\text{where } \vec{r}_\alpha = \frac{\vec{d}(\vec{\rho}_\alpha) - \vec{d}_{obs}}{\sqrt{\vec{d}(\vec{\rho}_\alpha)}} \quad \text{(S4)}$$

and $\mathbf{A}_\alpha = \mathbf{K}(\mathbf{K}^T\mathbf{K} + \alpha\mathbf{L})^{-1}\mathbf{K}^T$

Here $\vec{r}_\alpha$ is the regularized residual vector, σ^2 is the scalar variance of the noise in the data, and $\mathbf{A}_\alpha$ is called the influence matrix, which depends on a linear forward problem operator matrix $\mathbf{K}$ and a penalty operator $\mathbf{L}$. The value for σ^2 is taken to be 1 since the expected variance of the normalized residual is 1, since the expected variation of a Poisson random variable, x, is $\sqrt{x}$. The optimal value of α according to this method is that which minimizes Eq. (S4). Since neither $\mathbf{K}$ nor $\mathbf{L}$ can be directly computed from the problem, they both must be approximated. The forward problem operator $\mathbf{K}$ was approximated with the Jacobian of the forward problem at the regularized solution, $\mathbf{J}(\vec{\rho}_\alpha)$. The penalty operator used was a representation of the total variation regularization term

$$\boldsymbol{L} = \sqrt{(\boldsymbol{D}_i)^2 + (\boldsymbol{D}_j)^2 + \beta} \quad \text{(S5)}$$

This selection of the penalty operator was found to perform better than other linearizations tested, including the Jacobian and the Hessian of the regularization term.

An example of how α can be selected using UPRE as well as two other commonly used selections methods, generalized cross-validation (GCV) and the discrepancy principle (DP), can be found in the supplementary information of [3].

Supplementary Note 3. Radiography setup. A 1/2 in. stainless steel filter was put on the source in order to increase the average energy of the X-ray spectra to obtain increased transmission through the dense steel spheres. Seven source spectra were used in the inspection with endpoint energies of {150, 200, 250, 300, 350, 400, 450} keV and corresponding currents of {5.0, 3.6, 3.4, 2.5, 1.7, 1.25, 1.0} mA. Here 'endpoint energy' refers to the accelerator voltage of the X-ray source. Variable exposure times were used for the various endpoint energies in order to best use the available dynamic range on the detector. Five second exposures were used for the 150 and 200 keV endpoint energies, a 2.5 second exposure for the 250 keV endpoint energy, and 2 second exposures for the endpoints of 300 keV and above. In order to reduce the variability from one exposure to the next, the image data used in the analysis was an average of 32 individual exposures, for a varied total exposure time depending on the endpoint of the spectra, from about 1 minute to 2.5 minutes. For data analysis, subsets of the data from the seven endpoints were used.

Supplementary Note 4. Estimation of the scattered flux. The estimation of scattered flux on the image plane $\Phi_{scatter}$ used in Eq. (1) was completed using the same step wedge data shown in Fig. S1. Here, simulated data using simple ray-tracing is generated using the known step wedge materials and locations in the image data. Also, the spatial resolution is modeled by applying the convolution operators determined in Supplementary Note 1. Specifically, Eq. (2) is used to model the data with the known set of material thicknesses. The simulated data is then compared to the observed radiography data and the scatter term at each pixel is determined to be that which gives the best fit of the observed data to that modeled.

Using only the pixels that have heavy attenuation, such as those behind the lead and steel step wedges, a 2D polynomial is fit to these estimated scatter values to generate the $\Phi_{scatter}$ used in Eq. (1). An example of the resulting scatter estimate across the image plane is shown in Fig. S3. Note, the scatter contribution appears lowest in the center of the image, which is consistent with Monte Carlo image simulations. The scatter

contribution in the center of the image varies between 0.05 to 0.08, increasing for higher endpoint energies.

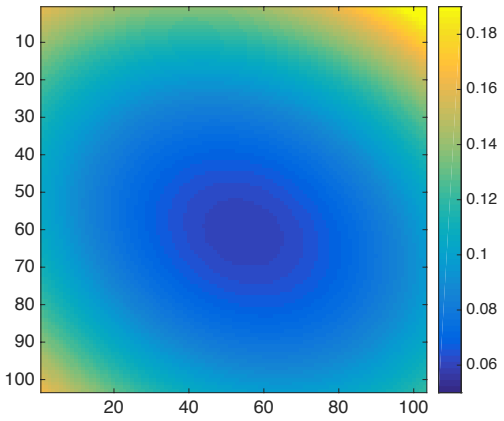

Figure S3: The estimated scatter term $\Phi_{scatter}$ *for the 250 keV endpoint energy data, given as a fraction of the incident flux.*

References

1. C. R. Vogel, *Computational Methods for Inverse Problems*. (SIAM, Philadelphia, 2002).
2. J. M. Bardsley and J. Goldes, "Regularization parameter selection methods for ill-posed Poisson maximum likelihood estimation," Inverse Problems **25** (9), 18 (2009).
3. Gilbert, A.J., B.S. McDonald, S.M. Robinson, K.D. Jarman, T.A. White, M.R. Deinert, *Non-invasive material discrimination using spectral x-ray imaging*. Journal of Applied Physics, 2014. **115**: p. 154901.